


 Cite this: *RSC Adv.*, 2020, 10, 25155

# Recyclable $MFe_2O_4$ ( $M = Mn, Zn, Cu, Ni, Co$ ) coupled micro–nano bubbles for simultaneous catalytic oxidation to remove $NO_x$ and $SO_2$ in flue gas

 Hongrui Sun and Dengxin Li \*

$NO_x$  can be efficiently removed by micro–nano bubbles coupling with  $Fe^{3+}$  and  $Mn^{2+}$ , but the catalyst cannot be reused and the adsorption wastewater should be treated. This work developed a new technology that uses micro–nano bubbles and recyclable  $MFe_2O_4$  to simultaneously remove  $NO_x$  and  $SO_2$  from flue gas, and clarified the effectiveness and reaction mechanism.  $MFe_2O_4$  ( $M = Mn, Zn, Cu, Ni$  and  $Co$ ) prepared by a hydrothermal method was characterized. The results show that  $MFe_2O_4$  can be activated to produce  $\cdot OH$  which can accelerate the oxidation absorption of  $NO_x$ . Compared with no catalyst, the  $NO_x$  conversion rate increased from 32.85% to 83.88% in the  $NO_x$ – $SO_2$ – $MFe_2O_4$ –micro–nano bubble system, while the removal rate of  $SO_2$  can reach 100% at room temperature. The catalytic activities of  $MFe_2O_4$  showed the following trend:  $CuFe_2O_4 > ZnFe_2O_4 > MnFe_2O_4 > CoFe_2O_4 > NiFe_2O_4$ . The results provide a new idea for the application of advanced oxidation processes in flue gas treatment.

 Received 17th May 2020  
 Accepted 20th June 2020

DOI: 10.1039/d0ra04392c

[rsc.li/rsc-advances](http://rsc.li/rsc-advances)

## 1. Introduction

With the development of industry, nitrogen oxides ( $NO_x$ ) and sulfur dioxide ( $SO_2$ ) have become the most common atmospheric pollutants.<sup>1,2</sup> The emission of these pollutants causes various environmentally harmful effects such as acid rain, photochemical smog, ozone depletion and climate warming.<sup>3</sup> At present, the main methods to control  $NO_x$  in industry are dry denitration technology and wet denitration technology. Dry denitrification techniques include selective catalytic reduction (SCR) and selective non-catalytic reduction (SNCR).<sup>4–6</sup> Wet denitrification techniques include oxidation, complexation absorption and acid–base absorption.<sup>7–9</sup> There are many kinds of pollutants in the actual flue gas, which make it difficult to deal with. It is a new trend to study the oxidation and absorption of various pollutants in flue gas by simple devices.<sup>10</sup> Flue gas desulfurization and denitrification integration refers to the process of simultaneous desulfurization and denitrification in the same equipment. Although this method can effectively improve the flue gas treatment efficiency and reduce the energy consumption, the main research is still in the research and development stage, there is still a long way to go before the large-scale industrialization. Micro–nano bubbles (MNB) coupled oxygen carrier (OCs) technology is a wet flue gas integrated removal technology, which can simplify the system,

reduce the cost, and ensure a high removal efficiency of  $NO_x$  and  $SO_2$ ,<sup>11,12</sup> and has a strong application potential. It is a new direction of the comprehensive removal of multi-pollutant flue gas.<sup>13</sup>

Micro–nano bubble technology refers to the bubble with the diameter between tens of microns to hundreds of nanometers when the bubble occurs.<sup>14</sup> Compared with ordinary bubbles, it has the following characteristics: small size leads to large surface area, low rising speed, high internal pressure, large gas solubility, and free radicals formed when crushed.<sup>13,15</sup> Hydroxyl radicals generated by the breakdown of micro–nano bubbles are an important reactive oxygen species with an oxidation potential of 2.8V.<sup>16–18</sup> Xiao<sup>19</sup> *et al.* used micro–nano bubbles to remove  $SO_2$  and  $NO$  ( $1000 \text{ mg m}^{-3}$ ), and  $NO$  removal efficiency reached 87.7%. It is well known that  $Fe^{2+}$  ions can promote the interaction between  $NO_x$  and  $S(IV)$  in aqueous solution to form nitrosyl complexes, which lead to enhanced  $NO_x$  removal.<sup>20,21</sup> Although the activation of transition metals can accelerate the oxidative absorption of  $NO_x$ , it is not suitable for recycling, and the product is heavy metal wastewater that causes secondary pollution. Therefore, it is necessary to use magnetic solid catalyst instead of ionic catalyst.

Previous studies have shown that spinel ferrite (chemical formula:  $M^{2+}Fe_2^{3+}O_4$ ) has better mechanical stability, stronger mechanical strength, reoxidation ability and environmental friendliness than single metal oxide.<sup>22–24</sup> In actual use,  $MFe_2O_4$  have acted as an oxygen supply and a catalyst.<sup>25,26</sup> The standard spinel structure is a lattice composed of 32 divalent oxygen ions that form a closed-pack, face-centered cubic arrangement with

School of Environmental Science and Engineering, Donghua University, 2999 North Renmin Road, Shanghai 201620, China. E-mail: lidengxin@dhu.edu.cn; Fax: +86 21 67792522; Tel: +86 13 636641041



64 tetrahedral interstitial sites and 32 octahedral interstitial sites.<sup>27</sup> In the spinel structure,  $M^{2+}$  and  $Fe^{3+}$  are respectively located in the sites of tetrahedron or octahedron composed of oxygen and have metal synergistic effects which determine good oxygen transferability and catalysis properties.<sup>28,29</sup> Therefore, spinel ferrites were attractive candidates because of their rich crystal chemistry, low cost, nontoxicity and environmentally friendly properties.<sup>30,31</sup> Xu *et al.*<sup>32</sup> found that a small quantity of palladium-doped ferrite spinel could achieve high NO conversion and the catalyst cost reduction. However, the simultaneous use of transition metal oxide and MNB for  $NO_x$  removal in a system has rarely been reported. Furthermore, the synergistic effects of the different metals in ferrites for NO and  $SO_2$  removal have been rarely mentioned.

In this study, the recyclable catalyst  $MFe_2O_4$  ( $M = Mn, Co, Ni, Cu, Zn$ ) synthesized with hydrothermal method and MNB were used to form the  $NO_x-SO_2-MFe_2O_4-MNB$  system for simultaneous removal of  $NO_x$  and  $SO_2$  from flue gas. The structural, physical, and chemical properties of the as-prepared  $MFe_2O_4$  before and after the reaction were characterized by X-ray diffraction (XRD), scanning electron microscopy (SEM), the Brunauer-Emmett-Teller (BET) method and X-ray photoelectron spectroscopy (XPS). The removal rates of NO and  $SO_2$  were monitored with the flue gas analyzer and ion chromatography to explore the actions of MNB and the effects of various divalent cations contained in the ferrite. The goal of this study was to evaluate the simultaneous NO and  $SO_2$  removal efficiencies, and elucidate the chemistry and reaction pathways of the  $NO_x-SO_2-MFe_2O_4-MNB$  system.

## 2. Experimental

### 2.1. Materials

All the materials used for synthesizing catalysts, including ethylene glycol, poly(ethylene glycol) (PEG), sodium acetate ( $CH_3COONa$ ), ferric chloride ( $FeCl_3 \cdot 6H_2O$ ), manganese chloride ( $MnCl_2 \cdot H_2O$ ), zinc chloride ( $ZnCl_2$ ), cupric chloride ( $CuCl_2 \cdot 2H_2O$ ), nickel chloride ( $NiCl_2 \cdot 6H_2O$ ), cobalt chloride ( $CoCl_2 \cdot 6H_2O$ ), ethyl alcohol ( $C_2H_6O$ ), 5,5-dimethyl-1-pyrroline N-oxide (DMPO), were purchased from Sinopharm Chemical Reagent Co., Ltd. All chemicals were used without further purification.

### 2.2. Synthesis of $MFe_2O_4$ ( $M = Mn, Co, Ni, Cu$ and $Zn$ ) by the hydrothermal method

The  $MFe_2O_4$  ( $M = Mn, Co, Ni, Cu$  and  $Zn$ ) microspheres were synthesized based on the hydrothermal method. Briefly, polyethylene glycol and sodium acetate were added into ethylene glycol under vigorous stirring conditions. Then partial chloride was added to reach the metal cation ( $Fe^{3+}$  and  $M^{2+}$ ) molar ratio of 2 : 1. The resultant homogeneous solution was obtained and then placed into the 500 mL Teflon-lined autoclave, reacted at 200 °C for 10 h. The black product was collected with a magnet, washed several times by ethanol and distilled water, and then dried at 80 °C for 6 h under vacuum. Finally, the resulting product was sufficiently grinded to obtain fresh  $MFe_2O_4$  ( $M = Mn, Co, Ni, Cu$  and  $Zn$ ).

### 2.3. Characterization

A scanning electron microscope (SEM, Hitachi S4800) was adopted to observe the morphologies. Energy dispersive spectrometer (EDS) with Horiba 7593-H was used to confirm the proportion of each element in the catalysts. Powder X-ray diffraction meter (XRD, D/max 2550 PC, Japan Rigaku) operation was completed with Cu  $K_\alpha$  radiation in a  $2\theta$  angle between 10° and 80° at a rate of 2°  $min^{-1}$  to monitor crystal structure. The surface properties and valence state of the catalysts were determined through X-ray photoelectron spectroscopy (XPS) experiments by using the Escalab 250Xi spectrometer with an Al- $K_\alpha$  radiation source at an energy step size of 1 eV to obtain high-resolution XPS spectra. The spectra were calibrated with respect to C 1s at a binding energy of 284.8 eV. The specific surface area of the samples was determined by using the Brunauer-Emmett-Teller (BET) method on an automated area and pore size analyzer (Autosorb-iQ) based on nitrogen adsorption desorption isotherm. The samples were outgassed at 200 °C for 2 h to remove remaining moisture and then analyzed with  $N_2$  gas as an adsorbent at the temperature of liquid nitrogen.  $\cdot OH$  and  $\cdot O_2^-$  in the  $NO_x-SO_2-MFe_2O_4-MNB$  system were detected *via* electron paramagnetic resonance spectroscopy (EPR, JEOL-FA200), and DMPO was used for capturing  $\cdot OH$  and  $\cdot O_2^-$ .

### 2.4. Reactivity measurement in the $NO_x-SO_2-MFe_2O_4-MNB$ system

Fig. 1 shows the  $NO_x-SO_2-MFe_2O_4-MNB$  system installation diagram. Firstly,  $NO_x$  and  $SO_2$  in the cylinder are fed into the mixer in a certain proportion to mix evenly. Gas flow rate is controlled by the rotameter. The flue gas analyzer (Testo350) was adopted to observe the intake gas concentration. Then a certain amount of  $MFe_2O_4$  is uniformly dispersed in the absorption solution by ultrasonic oscillation. Finally, the configured gas and absorption solution are passed through the micro-nano bubble generator together to form the  $NO_x-SO_2-MFe_2O_4-MNB$  system in the reaction tower, so as to complete the catalytic oxidation and absorption process of  $NO_x$  and  $SO_2$ . The removal efficiency of  $NO_x$  was calculated by the concentrations of  $NO_2^-$  and  $NO_3^-$  in the absorption liquid measured with ion chromatography (ICS-1100 AS11-HC, Thermo Fisher Scientific).

The rated parameters of the micro-nano bubble generator were set as follows: the effluent pressure (0.5 MPa), the inlet water flow (300  $mL\ min^{-1}$ ) and the intake air amount (48  $mL\ min^{-1}$ ). The volume of the oxidation absorption reactor is 1.5 L.  $MFe_2O_4$  was uniformly dispersed in a tubular reactor as a catalyst. A gas mixture containing 5113  $mg\ m^{-3}$   $NO_x$  and 3371  $mg\ m^{-3}$   $SO_2$  was used as the intake gas.  $NO_x$  is mainly composed of 3795  $mg\ m^{-3}$  NO and 2021  $mg\ m^{-3}$   $NO_2$ . In order to explore the practical application performance of the  $NO_x-SO_2-MFe_2O_4-MNB$  system, the effects of the addition of different recyclable  $MFe_2O_4$  catalysts on the integrated desulfurization and denitrification efficiency were discussed by analyzing the IC test results of the absorption solution.



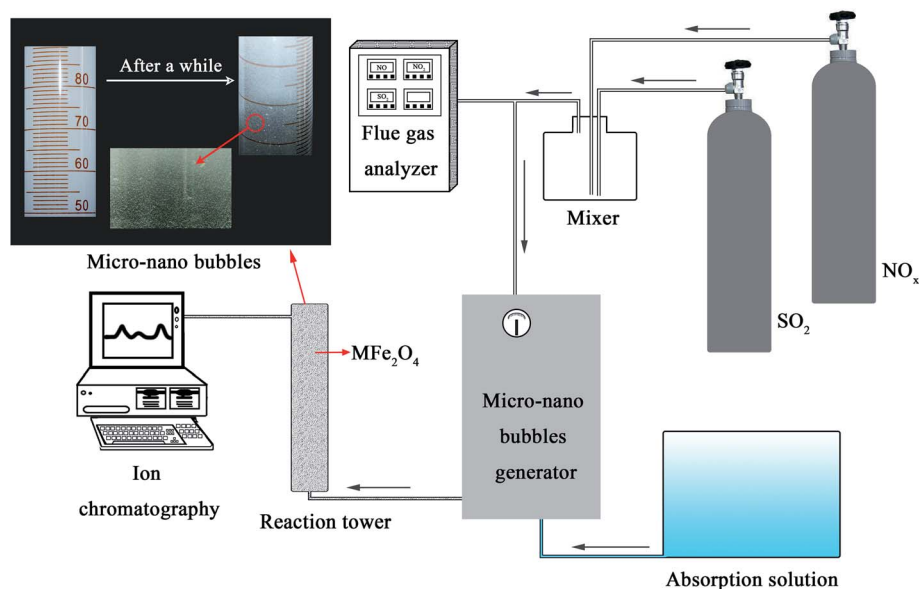


Fig. 1 The  $\text{NO}_x$ - $\text{SO}_2$ - $\text{MFe}_2\text{O}_4$ -MNB system installation diagram.

## 2.5. Analysis methods

The removal efficiency of  $\text{NO}_x$  can be calculated as

$$\eta_{\text{NO}_x} = \frac{N_{\text{out}}}{N_{\text{in}}} \times 100\% \quad (1)$$

$$N_{\text{in}} = \frac{c_{\text{NO}} \times q \times t}{M_{\text{NO}}} + \frac{c_{\text{NO}_2} \times q \times t}{M_{\text{NO}_2}} \quad (2)$$

$$N_{\text{out}} = \frac{c_{\text{NO}_2^-} \times V}{M_{\text{NO}_2^-}} + \frac{c_{\text{NO}_3^-} \times V}{M_{\text{NO}_3^-}} \quad (3)$$

where  $\eta_{\text{NO}_x}$  represents the removal efficiency of  $\text{NO}_x$ ,  $N_{\text{out}}$  is the amount of  $\text{NO}_2^-$  and  $\text{NO}_3^-$  in the absorption liquid,  $N_{\text{in}}$  is the amount of  $\text{NO}_x$  entering the system,  $c_{\text{NO}}$  and  $c_{\text{NO}_2}$  are the concentrations of  $\text{NO}$  and  $\text{NO}_2$  in the intake air respectively,  $c_{\text{NO}_2^-}$  and  $c_{\text{NO}_3^-}$  are the concentrations of  $\text{NO}_2^-$  and  $\text{NO}_3^-$  in the absorption liquid respectively,  $q$  is the air inflow,  $V$  is the volume of water in the reaction tower,  $M$  is the molecular weight,  $t$  is the system running time.

The removal efficiency of  $\text{SO}_2$  can be calculated as

$$\eta_{\text{SO}_2} = \frac{N'_{\text{out}}}{N'_{\text{in}}} \times 100\% \quad (4)$$

$$N'_{\text{in}} = \frac{c_{\text{SO}_2} \times q \times t}{M_{\text{SO}_2}} \quad (5)$$

$$N'_{\text{out}} = \frac{c_{\text{SO}_4^{2-}} \times V}{M_{\text{SO}_4^{2-}}} \quad (6)$$

where  $\eta_{\text{SO}_2}$  represents the removal efficiency of  $\text{SO}_2$ ,  $N'_{\text{out}}$  is the amount of  $\text{SO}_4^{2-}$  in the absorption liquid,  $N'_{\text{in}}$  is the amount of  $\text{SO}_2$  entering the system,  $c_{\text{SO}_2}$  are the concentrations of  $\text{SO}_2$  in the intake air,  $c_{\text{SO}_4^{2-}}$  are the concentrations of  $\text{SO}_4^{2-}$  in the absorption liquid.

## 3. Results and discussion

### 3.1. Physicochemical characterization

The SEM images of  $\text{MFe}_2\text{O}_4$  ( $M = \text{Mn}, \text{Zn}, \text{Cu}, \text{Ni}$  and  $\text{Co}$ ) are shown in Fig. 2. The five spinel ferrites are similar to each other, exhibiting a spherical structure with a dense surface and abundant fine particles. Among the five OCs,  $\text{CuFe}_2\text{O}_4$  and  $\text{CoFe}_2\text{O}_4$  exhibited more agglomeration and sintering, possibly due to high temperature calcination and the small-dimension effect. Compared with  $\text{CuFe}_2\text{O}_4$  and  $\text{CoFe}_2\text{O}_4$ ,  $\text{MnFe}_2\text{O}_4$ ,  $\text{NiFe}_2\text{O}_4$  and  $\text{ZnFe}_2\text{O}_4$  are spherical with the uniform shape and distribution. Fig. 2 gives a detailed description of  $\text{MFe}_2\text{O}_4$ .  $\text{MFe}_2\text{O}_4$  with the grain diameter of 100–350 nm. Among them,  $\text{CoFe}_2\text{O}_4$  and  $\text{CuFe}_2\text{O}_4$  had the smallest average particle sizes (127 nm for  $\text{CoFe}_2\text{O}_4$  and 151 nm for  $\text{CuFe}_2\text{O}_4$ ), which might be the cause for their relatively serious agglomeration. The particle sizes of various  $\text{MFe}_2\text{O}_4$  showed the following decreasing sequence:  $\text{MnFe}_2\text{O}_4 > \text{ZnFe}_2\text{O}_4 > \text{NiFe}_2\text{O}_4 > \text{CuFe}_2\text{O}_4 > \text{CoFe}_2\text{O}_4$ .

EDS analysis results (shown in Table 1) confirmed that the component contents of the samples are in reasonable agreement with the atomic percentages deduced from their molecular formulas. The elemental composition in Table 1 indicates that there are only three elements (O, M and Fe) in the composite. Furthermore, the M/Fe molar ratios of samples were approximately 0.5. The contents of the three elements in each complex  $\text{MFe}_2\text{O}_4$  were  $10.48 \pm 0.99\%$  (M, at%) and  $22.18 \pm 0.42\%$  (Fe, at%), respectively.

Table 1 shows the specific surface areas of the five spinel catalysts. The five ferrites exhibited different specific surface areas due to their different metal compositions. Among the five OCs,  $\text{CoFe}_2\text{O}_4$  had the largest specific surface area ( $121.352 \text{ m}^2 \text{ g}^{-1}$ ), followed by  $\text{NiFe}_2\text{O}_4$  ( $72.727 \text{ m}^2 \text{ g}^{-1}$ ). The ferrites of  $\text{MnFe}_2\text{O}_4$ ,  $\text{CuFe}_2\text{O}_4$  and  $\text{ZnFe}_2\text{O}_4$  had the smallest specific surface areas (less than  $30 \text{ m}^2 \text{ g}^{-1}$ ). The smaller the diameter of



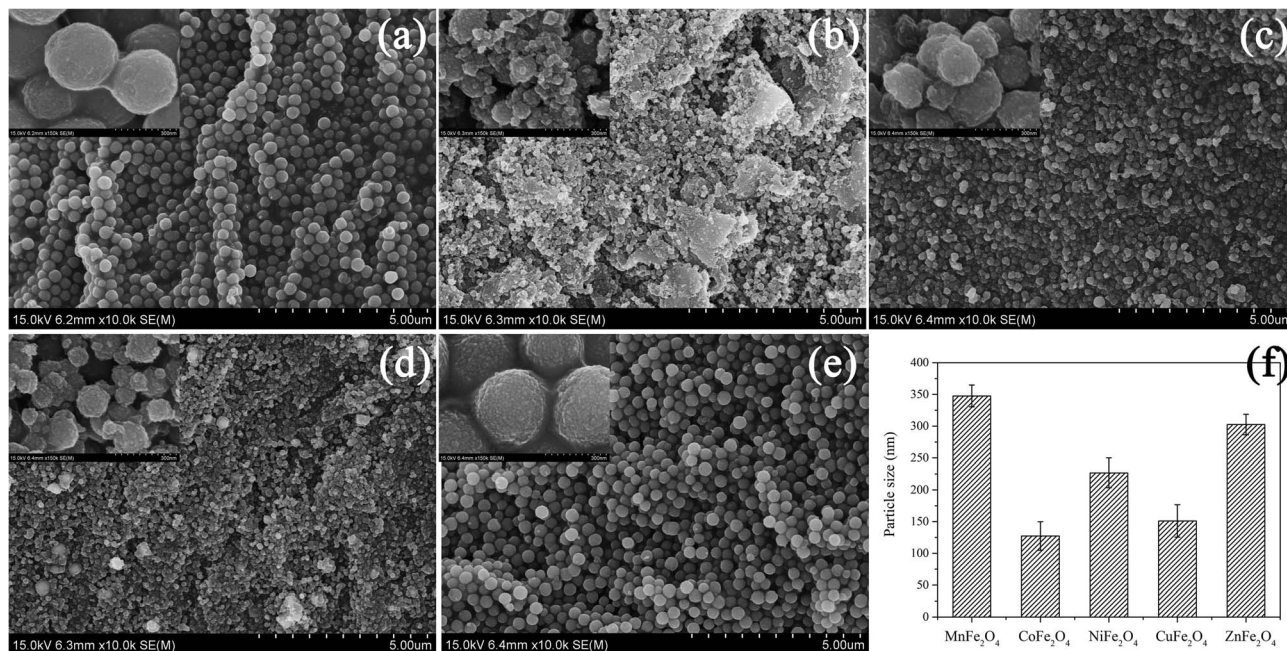


Fig. 2 SEM images of  $MFe_2O_4$ : (a)  $MnFe_2O_4$ , (b)  $CoFe_2O_4$ , (c)  $NiFe_2O_4$ , (d)  $CuFe_2O_4$  and (e)  $ZnFe_2O_4$  (f) size distributions of  $MFe_2O_4$  nanoparticles.

$MFe_2O_4$  nanoparticles was, the larger the specific surface area was (Fig. 2f and Table 1).

XRD measurements were conducted to identify the crystal structures of the samples. The XRD patterns of  $MFe_2O_4$  ( $M = Mn, Zn, Cu, Ni$  and  $Co$ ) are shown in Fig. 3. X-ray powder diffraction patterns of  $MnFe_2O_4$ ,  $CoFe_2O_4$ ,  $NiFe_2O_4$  and  $ZnFe_2O_4$  samples were quite similar to those of cubic spinel-type structures belonging to the  $Fd\bar{3}m$  (227) space group. The main diffraction reflection peaks included (220), (311), (400), (422), (511) and (440) crystal planes, which well matched with the standard XRD pattern representing the cubic spinel structure (JCPDS no. 38-0430, 22-1086, 10-0325, 34-0425 and 10-1108), indicating the good crystallinity of these  $MFe_2O_4$ .<sup>33</sup> Unlike these samples, however,  $CuFe_2O_4$  exhibited a well-defined spinel ferrite structure with a strongest peak reflection peak at the plane (211) that matched well with the standard XRD pattern (JCPDS no. 34-0425) representing a tetragonal system (space group:  $I4_1/amd$ ).<sup>34</sup>

The crystallite size  $D$  for each sample was estimated according to the most intense reflection peak (311) with Scherrer's equation (eqn (7)).<sup>35</sup>

$$D = \frac{K\lambda}{\beta \cos \theta} \quad (7)$$

where  $D$  is the average crystallite size;  $K$  is Scherrer constant, 0.89; corresponds to the wavelength of  $Cu-K\alpha$  radiation, 0.154 nm;  $\beta$  is the full width at half maximum intensity for a reflection maximum;  $\theta$  is the diffraction angle.

With Scherrer's Equation, crystallite sizes of  $MFe_2O_4$  nano-composites were calculated to be 13 nm (Table 1). The crystallite sizes of these OCs ranged from 10.07 to 15.94 nm. The crystallite sizes of the five  $MFe_2O_4$  showed the following decreasing sequence:  $MnFe_2O_4 > ZnFe_2O_4 > CuFe_2O_4 > CoFe_2O_4 > NiFe_2O_4$ . As the crystal grains of OCs increased, the crystallinity became better, but the probability of agglomeration also increased.  $CoFe_2O_4$  and  $NiFe_2O_4$  were most prone to agglomerate because of their smallest grain sizes, which were consistent with the SEM results (Fig. 2).

In order to give an insight into the elemental chemical valence and electronic properties on the surface layers of  $MFe_2O_4$ , XPS measurements of  $MFe_2O_4$  before and after the reactions were conducted to examine the chemical compositions and electronic structures of the samples. Fig. 4 shows the

Table 1 Physical and chemical properties of the investigated spinel catalysts

Catalysts	$S_{BET}$ ( $m^2 g^{-1}$ )	Elemental composition (atomic percentage, %)			Crystallite size from XRD (nm)
		M cation (Mn/Zn/Cu/Ni/Co)	Fe	M/Fe	
$MnFe_2O_4$	22.243	10.83	22.26	0.487	15.94
$CoFe_2O_4$	121.352	11.94	22.72	0.458	11.61
$NiFe_2O_4$	72.727	10.21	21.63	0.472	10.07
$CuFe_2O_4$	30.009	9.24	21.92	0.422	12.78
$ZnFe_2O_4$	20.326	10.20	22.37	0.456	14.11



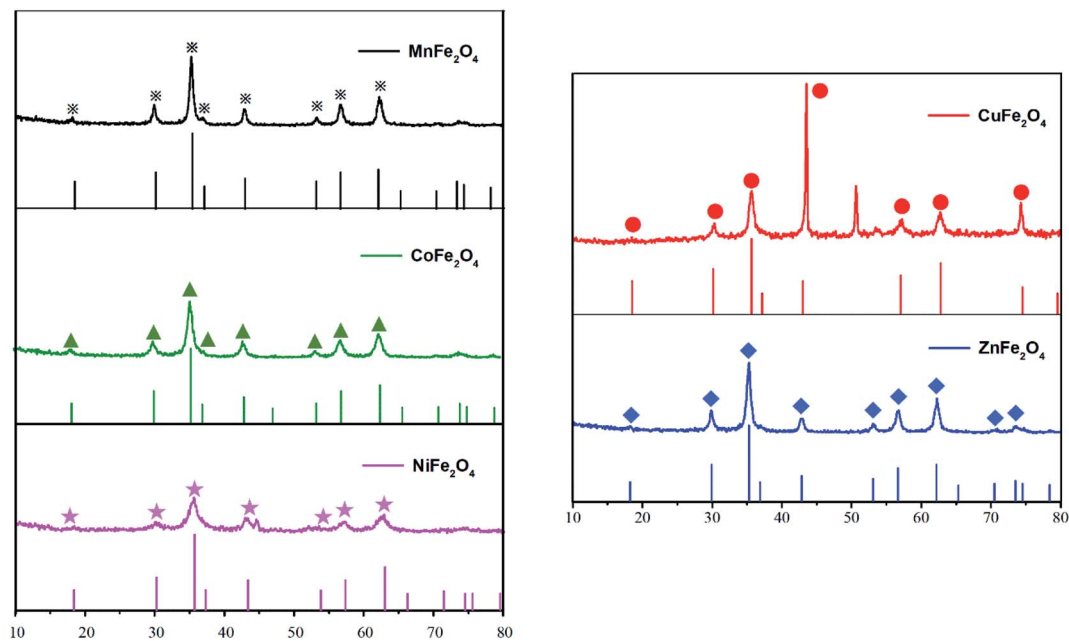


Fig. 3 XRD patterns of the investigated spinel catalysts  $MFe_2O_4$  and their standard profiles.

XPS spectra of  $MFe_2O_4$ , respectively. In full-scale XPS spectra (Fig. 4a), the apparent peaks of Fe 2p, C 1s, O 1s, Mn 2p, Co 2p, Ni 2p, Cu 2p and Zn 2p illustrated that iron, manganese, cobalt,

nickel, copper and zinc were the main elements of  $MFe_2O_4$ . The comparison of the peak differentiation-imitating analysis results of the nano- $MFe_2O_4$  before and after the reaction

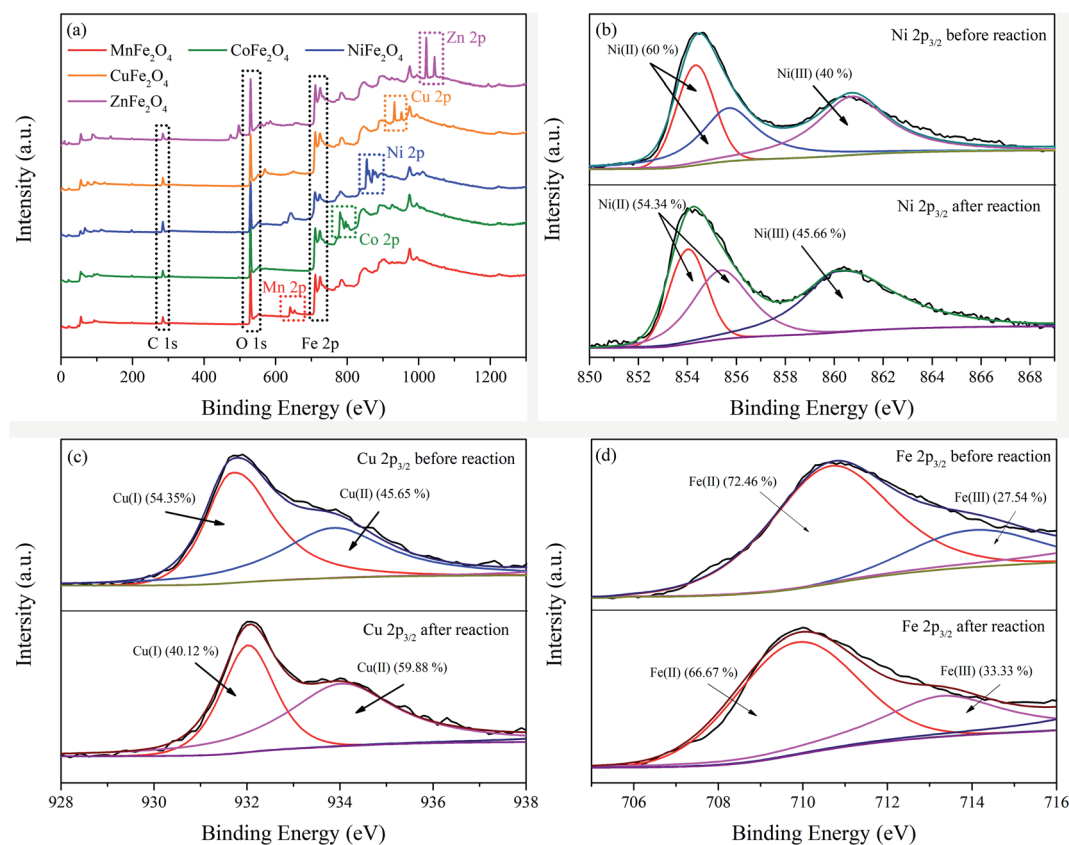


Fig. 4 XPS patterns of  $MFe_2O_4$  in the  $NO_x$ - $SO_2$ - $MFe_2O_4$ -MNB system before and after reactions: full-range scan of the samples (a), Ni  $2p_{3/2}$  (b), Cu  $2p_{3/2}$  (c), and Fe  $2p_{3/2}$  of  $ZnFe_2O_4$  (d).



(Fig. 4b–e) indicated that the binding energy of M 2p<sub>3/2</sub> was slightly reduced. After the reaction, the M(II) content in MFe<sub>2</sub>O<sub>4</sub> decreased, whereas the M(III) content increased with a variation range of 8.5 ± 4.03%. Fe 2p<sub>3/2</sub> was found to have characteristic peaks of Fe(II) and Fe(III) before the reaction, and the contents Fe(II) and Fe(III) were 72.46% and 27.53%, respectively. After the reaction, the contents of Fe(II) and Fe(III) were changed to 66.67% and 33.33% (Fig. 4f). The chemical states of Fe were changed in the catalytic process, so the catalyst always maintained a certain activity.<sup>36</sup> These results demonstrated that Fe and M elements were chemically cyclically converted during the catalytic oxidation of NO<sub>x</sub>, while generating active sites for free radicals.

### 3.2. Catalytic performance

The catalytic activities of the prepared samples of ZnFe<sub>2</sub>O<sub>4</sub> nanocomposites against NO<sub>x</sub> and SO<sub>2</sub> are shown in Fig. 5a. The ZnFe<sub>2</sub>O<sub>4</sub> addition amount of 0.02 g promoted the removal of NO<sub>x</sub> by the NO<sub>x</sub>-SO<sub>2</sub>-MFe<sub>2</sub>O<sub>4</sub>-MNB system, whereas the addition amount of 0.05 g inhibited the removal of NO<sub>x</sub>. The addition of trace catalysts can promote the oxidation absorption of NO<sub>x</sub>. However, excessive catalysts need to consume reactive oxygen species in the process of transformation to high price state, which forms a competitive relationship with the oxidation of NO<sub>x</sub> and SO<sub>2</sub>, resulting in the reduction of NO<sub>x</sub> removal rate. In addition, with the increase of the amount of additives, the particle catalyst and micro nano bubbles collide with each other, leading to a part of bubbles in advance rupture, unable to produce hydroxyl radicals, resulting in a reduction of NO<sub>x</sub> removal rate. Therefore, 0.02 g of iron-based spinel samples were separately added to the NO<sub>x</sub>-SO<sub>2</sub>-MFe<sub>2</sub>O<sub>4</sub>-MNB system.

The NO<sub>x</sub> removal efficiency is shown in Fig. 5b. The NO<sub>x</sub> removal efficiency of the NO<sub>x</sub>-SO<sub>2</sub>-MFe<sub>2</sub>O<sub>4</sub>-MNB system was improved after the addition of MFe<sub>2</sub>O<sub>4</sub>. The combined efficiency of MNB and MFe<sub>2</sub>O<sub>4</sub> in removing NO<sub>x</sub> reached 70.23 ± 10.63%, while the efficiency of SO<sub>2</sub> removal reached 100% (eqn (17)–(21)). Oxidative absorption of NO<sub>x</sub> involves two steps. NO<sub>x</sub> is firstly oxidized into NO<sub>2</sub><sup>-</sup>, which is then oxidized to NO<sub>3</sub><sup>-</sup> (eqn (13)–(16)). MnFe<sub>2</sub>O<sub>4</sub>, CuFe<sub>2</sub>O<sub>4</sub> and ZnFe<sub>2</sub>O<sub>4</sub> significantly

improved the efficiency of the second step. After adding CuFe<sub>2</sub>O<sub>4</sub>, the efficiency of converting NO<sub>x</sub> into NO<sub>2</sub><sup>-</sup> increased by 10.16%, and the conversion into NO<sub>3</sub><sup>-</sup> was 18.09%. Therefore, the comprehensive efficiency rate of NO<sub>x</sub> treatment by the NO<sub>x</sub>-SO<sub>2</sub>-CuFe<sub>2</sub>O<sub>4</sub>-MNB system reaches 83.88%. The catalytic activities showed the following decreasing sequence: CuFe<sub>2</sub>O<sub>4</sub> > ZnFe<sub>2</sub>O<sub>4</sub> > MnFe<sub>2</sub>O<sub>4</sub> > CoFe<sub>2</sub>O<sub>4</sub> > NiFe<sub>2</sub>O<sub>4</sub>.

### 3.3. Free radical identification

EPR test was conducted to detect the radicals and analyze the oxygen species of the NO<sub>x</sub>-SO<sub>2</sub>-MFe<sub>2</sub>O<sub>4</sub>-MNB system. As shown in Fig. 6a, weak signals were observed in MNB solution alone, and an intensive symmetrical four-line peak was detected in the NO<sub>x</sub>-SO<sub>2</sub>-MFe<sub>2</sub>O<sub>4</sub>-MNB system. The four-line peak with the intensity ratio of 1 : 2 : 2 : 1 in the spectrum is the typical spectral shape of the DMPO-<sup>•</sup>OH adducts,<sup>37</sup> which indicates the existence of <sup>•</sup>OH in the system. However, the characteristic 1 : 1 : 1 triplet assigned to DMPO-<sup>•</sup>O<sub>2</sub><sup>-</sup> adducts<sup>38</sup> formed by <sup>•</sup>O<sub>2</sub><sup>-</sup> and DMPO in Fig. 6b was very weak, indicating that the system mainly removes NO<sub>x</sub> through <sup>•</sup>OH instead of <sup>•</sup>O<sub>2</sub><sup>-</sup>. The intensity of the peak represents the concentration of <sup>•</sup>OH in the system, indicating that the concentration of <sup>•</sup>OH decreases in turn: MNB/CuFe<sub>2</sub>O<sub>4</sub> ≫ MNB > H<sub>2</sub>O. This result was consistent with the removal rate of NO<sub>x</sub>, which directly proved that <sup>•</sup>OH oxidized NO<sub>x</sub> is the key to denitrification of flue gas. It can also be proved that MFe<sub>2</sub>O<sub>4</sub> can be activated by MNB to produce <sup>•</sup>OH, which is dominant in the process of NO<sub>x</sub> removal.

### 3.4. Proposed reaction pathways

It can be found that the NO<sub>x</sub>-SO<sub>2</sub>-MFe<sub>2</sub>O<sub>4</sub>-MNB system has a high catalytic efficiency as a heterogeneous catalytic system, based on characterizing the physical and chemical properties of MFe<sub>2</sub>O<sub>4</sub> (M = Mn, Zn, Cu, Ni and Co) before and after the reaction and analyzing the SO<sub>2</sub> and NO<sub>x</sub> removal efficiency. Hydroxyl radical is the main oxidant during the chemical oxidation of SO<sub>2</sub> and NO<sub>x</sub> in aqueous solution. In this system, the sources of hydroxyl radicals are divided into two parts. Some hydroxyl radicals are derived from the rupture of MNB,<sup>39,40</sup> and the other part is derived from the activation of recyclable

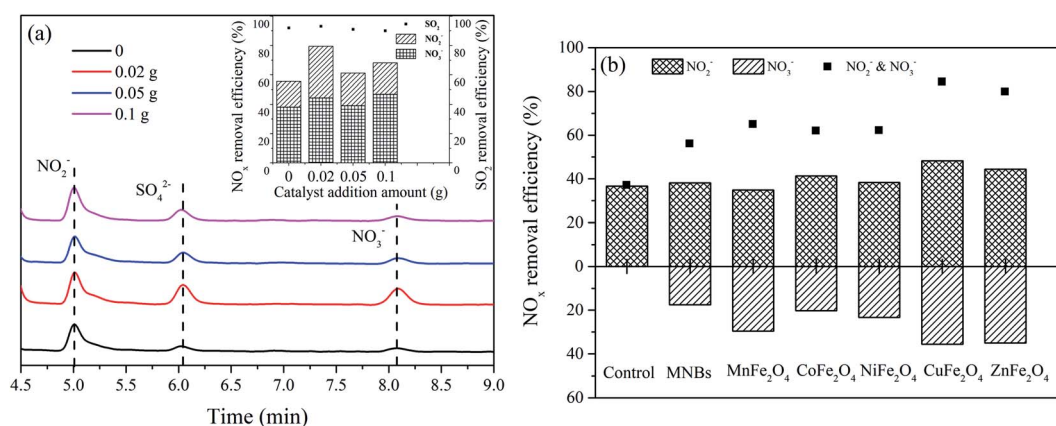


Fig. 5 Effect of spinel catalyst on NO<sub>x</sub> and SO<sub>2</sub> removal rate: ZnFe<sub>2</sub>O<sub>4</sub> (a), MFe<sub>2</sub>O<sub>4</sub> (b).



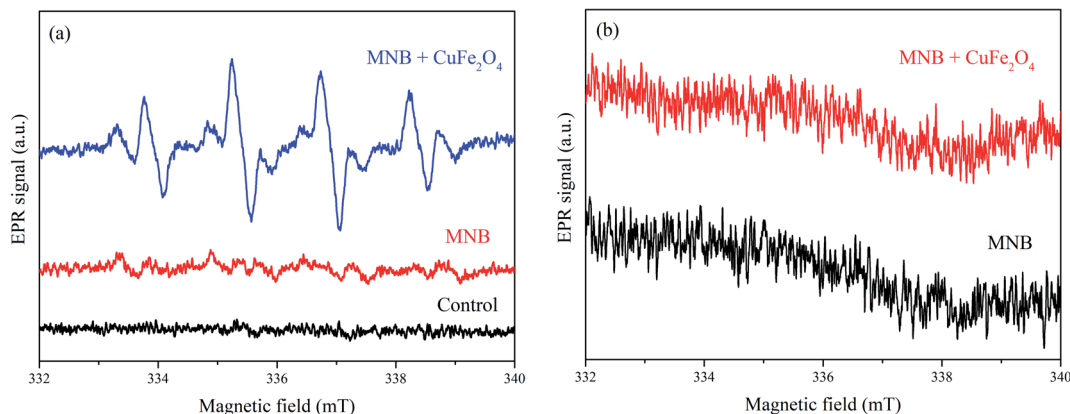


Fig. 6 EPR spectra of the  $\text{NO}_x\text{-SO}_2\text{-MFe}_2\text{O}_4\text{-MNB}$  system:  $\text{DMPO}\text{-}\cdot\text{OH}$  (a), and  $\text{DMPO}\text{-}\cdot\text{O}_2^-$  (b).

$\text{MFe}_2\text{O}_4$ . The chemistry of simultaneous oxidation of  $\text{NO}_x$  and  $\text{SO}_2$  by micro-nano bubbles breakdown and  $\text{MFe}_2\text{O}_4$  activation is complex, since it takes place through electron transfer from the lattice oxygen, free radical oxidation reactions *via*  $\cdot\text{OH}$  and  $\cdot\text{O}_2^-$ , and the direct reaction of the  $\text{NO}_x$  with  $\text{HSO}_3^-$ .<sup>41,42</sup>

The catalytic oxidation mechanism of  $\text{NO}_x\text{-SO}_2\text{-MFe}_2\text{O}_4\text{-MNB}$  system is described visually in the reaction scheme shown in Fig. 7. As the MNB slowly rise and shrink in the water, the charge ions ( $\text{H}^+$ ,  $\text{OH}^-$ ) rapidly concentrate at the very narrow gas-liquid interface. At the moment of MNB explosion, due to the drastic changes caused by the disappearance of the gas-liquid interface, the concentrated ions on the interface will immediately release the stored chemical energy, thus producing a large number of  $\cdot\text{OH}$ .  $\text{MFe}_2\text{O}_4$  is a magnetic semiconductor material with spinel structure. Oxygen in molecular state ( $\text{O}_2$ ) is adsorbed on the metal surface and then dissociated into

adsorbed atoms ( $\text{O}_{\text{ad}}$ ) because  $\text{MFe}_2\text{O}_4$  is magnetic.<sup>43</sup> The type I adsorbed oxygen atom ( $\text{O}_{\text{ad}}(\text{I})$ ) is first formed during dissociation, which is equivalent to a locally adsorbed oxygen atom on the metal surface. The oxygen atom in this state has extremely high reactivity to  $\text{NO}_x$ . In addition, as a semiconductor material,  $\text{MFe}_2\text{O}_4$  consists of a low energy valence band full of electrons and an empty high energy conduction band. In the excited state, the valence band electron jumps to the conduction band, which is called the conduction band electron ( $e_{\text{CB}}^-$ ). At the same time, a highly active hole in the valence band is generated, which is called the valence band electron hole ( $h_{\text{VB}}^+$ ). The electron hole pair produces a large number of reactive oxygen species such as hydroxyl free radicals and hydrogen peroxide free radicals on the material surface, as shown in eqn (8)–(12). Reactive oxygen species is the main oxidant in the process of removing  $\text{NO}_x$  and  $\text{SO}_2$ . According to the double reduction oxidation mechanism,

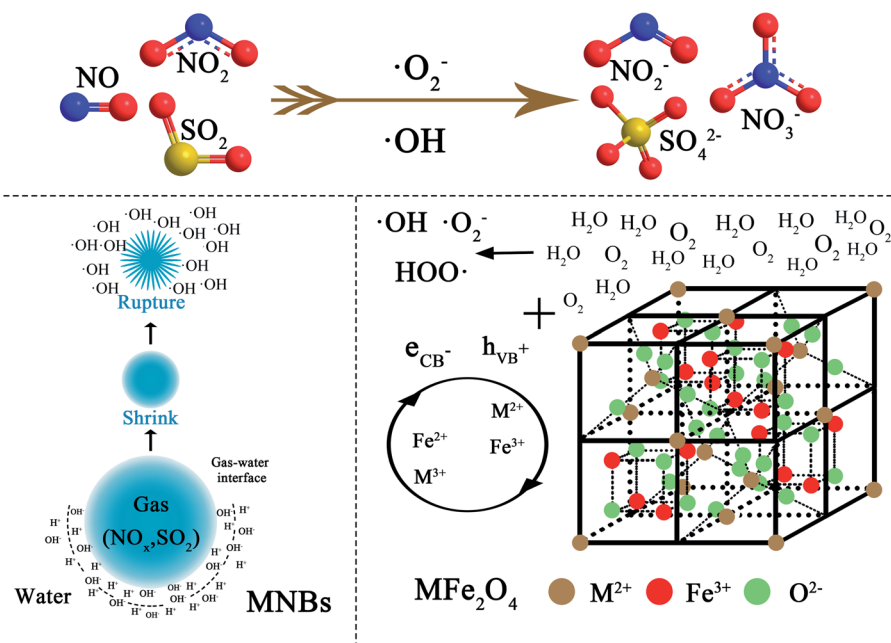
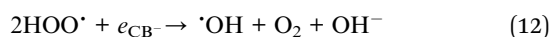
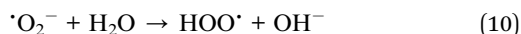
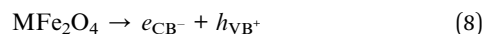


Fig. 7 Schematic diagram of the  $\text{NO}_x\text{-SO}_2\text{-MFe}_2\text{O}_4\text{-MNB}$  reacting system.

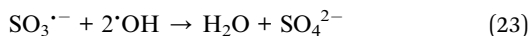
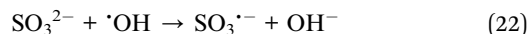
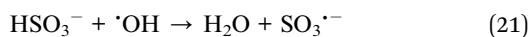
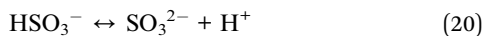
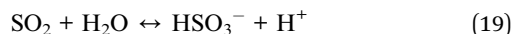
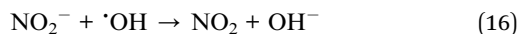
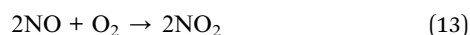


a kind of cations ( $\text{Fe}^{3+}$ ) perform the function of activating and oxidizing  $\text{NO}_x$  and  $\text{SO}_2$ , and their reoxidation depends on the lattice oxygen ( $\text{O}^{2-}$ ) transferred along the lattice. Another metal cation ( $\text{M}^{2+}$  ( $\text{M} = \text{Mn}, \text{Co}, \text{Ni}, \text{Cu}$  and  $\text{Zn}$ )) in the reduced state assumes the role of accepting gas-phase oxygen.

The main reactions involved in spinel catalytic oxidation are:



The main reactions involved in the simultaneous oxidation of  $\text{NO}_x$  and  $\text{SO}_2$  are:



## 4. Conclusion

This work developed a new technology that uses micro-nano bubbles and  $\text{MFe}_2\text{O}_4$  to simultaneously remove  $\text{NO}_x$  and  $\text{SO}_2$  from flue gas. The physicochemical properties of  $\text{MFe}_2\text{O}_4$  prepared by the hydrothermal method were characterized. The results indicated that both micro-nano bubbles and  $\text{MFe}_2\text{O}_4$  improved  $\text{NO}_x$  removal, while and the removal rate of  $\text{SO}_2$  can reach 100% at room temperature.  $\text{NO}_x$  removal rate reached 83.88% in  $\text{NO}_x$ - $\text{SO}_2$ - $\text{CuFe}_2\text{O}_4$ -MNB system. At the moment when the MNB burst, the concentrated ions on the gas-water interface will release the stored chemical energy at once, thus

producing a large number of hydroxyl radicals. Recyclable  $\text{MFe}_2\text{O}_4$  ( $\text{M} = \text{Mn}, \text{Zn}, \text{Cu}, \text{Ni}$  and  $\text{Co}$ ) can produce  $\cdot\text{OH}$  and  $\cdot\text{O}_2^-$  by being activated, thus accelerating the oxidation and absorption process of  $\text{NO}_x$  and  $\text{SO}_2$ . However, this research also points out many areas that require further research, such as using the system for organic gas and wastewater treatment, which is beyond the scope of current research, but is still the subject of future research.

## Conflicts of interest

There are no conflicts to declare.

## Acknowledgements

This work was supported by the National Natural Science Foundation of China [grant number U1660107], the Fundamental Research Funds for the Central Universities [grant number 2232020A-10].

## References

- 1 F. X. Qie, J. Y. Zhu, J. F. Rong and B. N. Zong, Biological removal of nitrogen oxides by microalgae, a promising strategy from nitrogen oxides to protein production, *Bioresour. Technol.*, 2019, **292**, 10.
- 2 D. L. Goldberg, Z. F. Lu, D. G. Streets, B. de Foy, D. Griffin, C. A. McLinden, L. N. Lamsal, N. A. Krotkov and H. Eskes, Enhanced capabilities of TROPOMI  $\text{NO}_2$ : estimating  $\text{NO}_x$  from north American cities and power plants, *Environ. Sci. Technol.*, 2019, **53**, 12594–12601.
- 3 K. H. Bates and D. J. Jacob, A new model mechanism for atmospheric oxidation of isoprene: global effects on oxidants, nitrogen oxides, organic products, and secondary organic aerosol, *Atmos. Chem. Phys.*, 2019, **19**, 9613–9640.
- 4 J. Q. Xu, H. J. Yu, C. Zhang, F. Guo and J. Q. Xie, Development of cerium-based catalysts for selective catalytic reduction of nitrogen oxides: a review, *New J. Chem.*, 2019, **43**, 3996–4007.
- 5 Z. Y. Wang, H. L. Kuang, J. F. Zhang, L. L. Chu and Y. L. Ji, Nitrogen oxide removal by non-thermal plasma for marine diesel engines, *RSC Adv.*, 2019, **9**, 5402–5416.
- 6 M. Jablonska and R. Palkovits, Perovskite-based catalysts for the control of nitrogen oxide emissions from diesel engines, *Catal. Sci. Technol.*, 2019, **9**, 2057–2077.
- 7 J. M. Shao, C. Q. Xu, Z. H. Wang, J. P. Zhang, R. T. Wang, Y. He and K. F. Cen,  $\text{NO}_x$  reduction in a 130 t/h biomass-fired circulating fluid bed boiler using coupled ozonation and wet absorption technology, *Ind. Eng. Chem. Res.*, 2019, **58**, 18134–18140.
- 8 J. Chen, Y. Chen, D. Hrynsphan, Y. Mei, H. Pan, J. L. Wu, J. M. Chen and J. C. Yao, Fe-II(EDTA)-NO reduction by Mn powder in wet flue gas denitrification technology coupled with  $\text{Mn}^{2+}$  recycling: performance, kinetics, and mechanism, *Energy Fuels*, 2020, **34**, 2590–2598.
- 9 X. Y. Zhu, F. Q. He, M. Xia, H. G. Liu and J. H. Ding, Evaluation of Fe(III)EDTA reduction with ascorbic acid in a wet denitrification system, *RSC Adv.*, 2019, **9**, 24386–24393.





- 10 J. Johansson, F. Normann, N. Sarajlic and K. Andersson, Technical-scale evaluation of scrubber-based, Co-removal of NO<sub>x</sub> and SO<sub>x</sub> species from flue gases via gas-phase oxidation, *Ind. Eng. Chem. Res.*, 2019, **58**, 21904–21912.
- 11 Z. G. Xiao, D. X. Li, F. K. Wang, Z. H. Sun and Z. Y. Lin, Simultaneous removal of NO and SO<sub>2</sub> with a new recycling micro-nano bubble oxidation-absorption process based on HA-Na, *Sep. Purif. Technol.*, 2020, **242**, 12.
- 12 Z. G. Xiao, D. X. Li, Q. L. Zhu and Z. H. Sun, Simultaneous removal of NO and SO<sub>2</sub> through a new wet recycling oxidation-reduction process utilizing micro-nano bubble gas-liquid dispersion system based on Na<sub>2</sub>SO<sub>3</sub>, *Fuel*, 2020, **263**, 10.
- 13 W. Fan, Z. Zhou, W. T. Wang, M. X. Huo, L. L. Zhang, S. Y. Zhu, W. Yang and X. Z. Wang, Environmentally friendly approach for advanced treatment of municipal secondary effluent by integration of micro-nano bubbles and photocatalysis, *J. Clean. Prod.*, 2019, **237**, 8.
- 14 S. Hamamoto, T. Takemura, K. Suzuki and T. Nishimura, Effects of pH on nano-bubble stability and transport in saturated porous media, *J. Contam. Hydrol.*, 2018, **208**, 61–67.
- 15 Y. X. Liu, Y. P. Zhou, T. Z. Wang, J. C. Pan, B. Zhou, T. Muhammad, C. F. Zhou and Y. K. Li, Micro-nano bubble water oxygation: Synergistically improving irrigation water use efficiency, crop yield and quality, *J. Clean. Prod.*, 2019, **222**, 835–843.
- 16 Y. F. Wu, H. Lin, W. Z. Yin, S. C. Shao, S. H. Lv and Y. Y. Hu, Water Quality and Microbial Community Changes in an Urban River after Micro-Nano Bubble Technology in Situ Treatment, *Water*, 2019, **11**, 14.
- 17 W. P. Zhang, G. Y. Li, H. L. Liu, J. Y. Chen, S. T. Ma and T. C. An, Micro/nano-bubble assisted synthesis of Au/TiO<sub>2</sub>@CNTs composite photocatalyst for photocatalytic degradation of gaseous styrene and its enhanced catalytic mechanism, *Environ. Sci.: Nano*, 2019, **6**, 948–958.
- 18 Z. R. Xia and L. M. Hu, Treatment of Organics Contaminated Wastewater by Ozone Micro-Nano-Bubbles, *Water*, 2019, **11**, 10.
- 19 Z. G. Xiao, T. Bin Aftab, X. L. Yuan, H. L. Xia and D. X. Li, Experimental results of NO removal by the MBGLS, *Micro & Nano Lett.*, 2019, **14**, 721–726.
- 20 O. S. Furman, A. L. Teel and R. J. Watts, Mechanism of base activation of persulfate, *Environ. Sci. Technol.*, 2010, **44**, 6423–6428.
- 21 Y. G. Adewuyi, N. Y. Sakyi and M. A. Khan, Simultaneous removal of NO and SO<sub>2</sub> from flue gas by combined heat and Fe<sup>2+</sup> activated aqueous persulfate solutions, *Chemosphere*, 2018, **193**, 1216–1225.
- 22 K. Q. Wang, B. L. Dou, B. Jiang, Q. Zhang, M. Li, H. S. Chen and Y. J. Xu, Effect of support on hydrogen production from chemical looping steam reforming of ethanol over Ni-based oxygen carriers, *Int. J. Hydrogen Energy*, 2016, **41**, 17334–17347.
- 23 S. Golchinfafa, S. M. Masoudpanah and M. Jazirehpour, Magnetic and microwave absorption properties of FeCo/CoFe<sub>2</sub>O<sub>4</sub> composite powders, *J Alloy Compd*, 2019, **809**, 7.
- 24 Y. Wang, X. Gao, X. M. Wu, W. Z. Zhang, C. Y. Luo and P. B. Liu, Facile design of 3D hierarchical NiFe<sub>2</sub>O<sub>4</sub>/N-GN/ZnO composite as a high performance electromagnetic wave absorber, *Chem. Eng. J.*, 2019, **375**, 10.
- 25 M. Taei, E. Havakeshian, H. Salavati and M. Azemati, Highly active electrocatalysts for ethanol oxidation based on gold nanodendrites modified with NiFe<sub>2</sub>O<sub>4</sub> nanoparticles decorated multi-walled carbon nanotubes, *Chem. Pap.*, 2019, **73**, 2687–2695.
- 26 J. G. Kim, Y. Noh, Y. Kim, S. Lee and W. B. Kim, Formation of ordered macroporous ZnFe<sub>2</sub>O<sub>4</sub> anode materials for highly reversible lithium storage, *Chem. Eng. J.*, 2019, **372**, 363–372.
- 27 E. Finley, M. W. Gaultois and J. Brgoch, Unlocking the key to persistent luminescence with X-ray absorption spectroscopy: a local structure investigation of Cr-substituted spinel-type phosphors, *Phys. Chem. Chem. Phys.*, 2019, **21**, 19349–19358.
- 28 X. C. Huang, J. Y. Zhang, M. Wu, S. Zhang, H. Y. Xiao, W. Q. Han, T. L. Lee, A. Tadich, D. C. Qi, L. Qiao, L. Chen and K. H. L. Zhang, Electronic structure and p-type conduction mechanism of spinel cobaltite oxide thin films, *Phys. Rev. B*, 2019, **100**, 9.
- 29 Y. Liu, D. P. Xu, T. Cui, H. M. Yu, X. F. Li and L. Li, Growth and properties of spinel structure Zn<sub>1.8</sub>Co<sub>0.2</sub>TiO<sub>4</sub> single crystals by the optical floating zone method, *RSC Adv.*, 2019, **9**, 26436–26441.
- 30 Y. F. Li, J. H. Shen, Y. J. Hu, S. J. Qiu, G. Q. Min, Z. T. Song, Z. Sun and C. Z. Li, General flame approach to chainlike MFe<sub>2</sub>O<sub>4</sub> spinel (M = Cu, Ni, Co, Zn) nanoaggregates for reduction of nitroaromatic compounds, *Ind. Eng. Chem. Res.*, 2015, **54**, 9750–9757.
- 31 T. Wang, J. Y. Wang, Y. M. Sun, Y. Duan, S. N. Sun, X. Hu, S. B. Xi, Y. H. Du, C. Wang and Z. C. J. Xu, Origin of electronic structure dependent activity of spinel ZnNi<sub>x</sub>Co<sub>2-x</sub>O<sub>4</sub> oxides for complete methane oxidation, *Appl. Catal. B-Environ.*, 2019, **256**, 9.
- 32 C. C. Xu, W. Sun, L. M. Cao and J. Yang, Highly efficient Pd-doped ferrite spinel catalysts for the selective catalytic reduction of NO with H<sub>2</sub> at low temperature, *Chem. Eng. J.*, 2016, **289**, 231–238.
- 33 J. Li, J. F. Yan, G. Yao, Y. H. Zhang, X. Li and B. Lai, Improving the degradation of atrazine in the three-dimensional (3D) electrochemical process using CuFe<sub>2</sub>O<sub>4</sub> as both particle electrode and catalyst for persulfate activation, *Chem. Eng. J.*, 2019, **361**, 1317–1332.
- 34 R. Z. Zhang, J. M. Liu, S. F. Wang, J. Z. Niu, C. G. Xia and W. Sun, Magnetic CuFe<sub>2</sub>O<sub>4</sub> Nanoparticles as an Efficient Catalyst for C-O Cross-Coupling of Phenols with Aryl Halides, *ChemCatChem*, 2011, **3**, 146–149.
- 35 J. H. Sui, C. Zhang, D. Hong, J. Li, Q. Cheng, Z. G. Li and W. Cai, Facile synthesis of MWCNT-ZnFe<sub>2</sub>O<sub>4</sub> nanocomposites as anode materials for lithium ion batteries, *J. Mater. Chem.*, 2012, **22**, 13674–13681.
- 36 Y. B. Ding, L. H. Zhu, N. Wang and H. Q. Tang, Sulfate radicals induced degradation of tetrabromobisphenol A with nanoscaled magnetic CuFe<sub>2</sub>O<sub>4</sub> as a heterogeneous catalyst of peroxymonosulfate, *Appl. Catal. B-Environ.*, 2013, **129**, 153–162.



- 37 B. C. Yang, S. X. Ma, R. J. Cui, S. J. Sun, J. Wang and S. C. Li, Simultaneous removal of  $\text{NO}_x$  and  $\text{SO}_2$  with  $\text{H}_2\text{O}_2$  catalyzed by alkali/magnetism-modified fly ash: High efficiency, low cost and catalytic mechanism, *Chem. Eng. J.*, 2019, **359**, 233–243.
- 38 Z. H. Meng, C. Y. Wang, X. R. Wang and H. Q. Li, Efficient and stable catalyst of  $\alpha\text{-FeOOH}$  for NO oxidation from coke oven flue gas by the catalytic decomposition of gaseous  $\text{H}_2\text{O}_2$ , *RSC Adv.*, 2020, **10**, 8207–8211.
- 39 M. Takahashi,  $\zeta$  potential of microbubbles in aqueous solutions: Electrical properties of the gas-water interface, *J. Phys. Chem. B*, 2005, **109**, 21858–21864.
- 40 M. Takahashi, K. Chiba and P. Li, Formation of hydroxyl radicals by collapsing ozone microbubbles under strongly acidic conditions, *J. Phys. Chem. B*, 2007, **111**, 11443–11446.
- 41 N. Chaibakhsh and Z. Moradi-Shoeili, Enzyme mimetic activities of spinel substituted nanoferrites ( $\text{MFe}_2\text{O}_4$ ): A review of synthesis, mechanism and potential applications, *Mater. Sci. Eng., C*, 2019, **99**, 1424–1447.
- 42 S. Chandrasekaran, C. Bowen, P. X. Zhang, Z. L. Li, Q. H. Yuan, X. Z. Ren and L. B. Deng, Spinel photocatalysts for environmental remediation, hydrogen generation,  $\text{CO}_2$  reduction and photoelectrochemical water splitting, *J. Mater. Chem. A*, 2018, **6**, 11078–11104.
- 43 W. K. Zhao, S. L. Zhang, J. Ding, Z. Y. Deng, L. Guo and Q. Zhong, Enhanced catalytic ozonation for  $\text{NO}_x$  removal with  $\text{CuFe}_2\text{O}_4$  nanoparticles and mechanism analysis, *J. Mol. Catal. A: Chem.*, 2016, **424**, 153–161.

